



PAPER

[View Article Online](#)
[View Journal](#) | [View Issue](#)Cite this: *Dalton Trans.*, 2024, **53**,
3685Silver frameworks based on a
tetraphenylethylene–imidazole ligand for
electrocatalytic reduction of CO₂ to CO†Yu-Jie Wang, Zhao-Feng Qiu, Ya Zhang, Fang-Fang Wang, Yue Zhao  and
Wei-Yin Sun *

Metal–organic frameworks (MOFs) can be used as electrocatalysts for the CO₂ reduction reaction (CO₂RR) because of their well-dispersed metal centers. Silver is a common electrocatalyst for reduction of CO₂ to CO. In this study, two Ag-MOFs with different structures of [Ag₈O₂(TIPE)₆](NO₃)₄ (**Ag-MOF1**) and [Ag(TIPE)_{0.5}CF₃SO₃] (**Ag-MOF2**) [TIPE = 1,1,2,2-tetrakis(4-(imidazol-1-yl)phenyl)ethene] were synthesized and used for CO₂ electroreduction. The results show that **Ag-MOF2** is superior to **Ag-MOF1** and exhibits high CO faradaic efficiency (FE) of 92.21% with partial current density of 29.51 mA cm^{−2} at −0.98 V versus reversible hydrogen electrode (RHE). The FE_{CO} is higher than 80% in the potential range of −0.78 to −1.18 V. The difference may be caused by different framework structures leading to different electrochemical active surface areas and charge transfer kinetics. This study provides a new strategy for designing and constructing CO₂ electroreduction catalysts and provides potential ways for solving environmental and energy problems caused by excessive CO₂ emission.

Received 5th December 2023,
Accepted 17th January 2024

DOI: 10.1039/d3dt04056a

rsc.li/dalton

Introduction

The environmental problems caused by rapid consumption of fossil fuels such as coal, oil and natural gas disrupt the carbon balance of nature.¹ Researchers have designed and developed a series of methods for storing and converting carbon dioxide (CO₂) to reduce its content in the atmosphere and thereby alleviate the greenhouse effect.^{2–4} It has been reported that CO₂ can be converted into usable high-value energy products or chemicals, which can simultaneously solve the problem of energy depletion.^{5,6} Due to the latest developments in renewable energy generation, such as solar and wind, the electrocatalytic CO₂ reduction reaction (CO₂RR) has become one of the most attractive pathways for CO₂ conversion due to its simple installation, high efficiency and low energy consumption.^{7,8} However, due to the chemical inertness of CO₂ and its high C=O chemical bond dissociation energy (~750 kJ mol^{−1}), the transformation of CO₂ needs to overcome considerable kinetic obstacles arising from the thermo-

dynamic stability and low electron affinity of CO₂.⁹ In addition, the process of electrocatalytic reduction of CO₂ is accompanied by the production of the competitive by-product H₂, which leads to a decrease in the faradaic efficiency of the catalyst.¹⁰ Therefore, development of efficient, highly selective and stable CO₂ electrocatalysts is the focus of current research works.¹¹

As a typical CO₂ reduction product, CO is of great significance for synthesizing carbon-based fuels and reducing CO₂ emissions. In addition, the reduction of CO₂ to CO has high selectivity and low separation cost. In the past few decades, electrocatalysts for CO₂RRs such as metals, non-metallic two-dimensional (2D) materials and metal–organic frameworks (MOFs) have been widely studied.^{9,12–14} Compared with traditional catalysts, MOFs composed of metal nodes and organic connectors have advantages, such as well-defined framework structures and well-dispersed metal centers,^{15–19} which are conducive to establishing accurate structure–activity relationships for the CO₂RR and exhibit excellent prospects in CO₂ electroreduction.^{20–22} However, the conductivity of MOFs is poor, and they cannot provide sufficient electrons during the CO₂ electrochemical reduction process. In addition, the hydrogen evolution reaction (HER) is a competitive reaction in the CO₂ electroreduction process; thus, inhibiting the HER is key to improving selectivity. Therefore, simultaneously assembling electron donating groups and active components for CO₂ electroreduction into MOFs to improve CO₂ electroreduction efficiency and selectivity is a major challenge at present. It has been reported that metals such as Ag, Zn and In, located on

Coordination Chemistry Institute, State Key Laboratory of Coordination Chemistry, School of Chemistry and Chemical Engineering, Nanjing National Laboratory of Microstructures, Collaborative Innovation Center of Advanced Microstructures, Nanjing University, Nanjing 210023, China. E-mail: sunwy@nju.edu.cn

† Electronic supplementary information (ESI) available: IR, PXRD, TG and other tables and figures. CCDC 2311795 and 2311796. For ESI and crystallographic data in CIF or other electronic format see DOI: <https://doi.org/10.1039/d3dt04056a>

the left branch of the Trassati volcanic curve, are valid catalysts with high CO₂RR selectivity.^{10,23,24}

Inspired by the above-mentioned considerations, 1,1,2,2-tetrakis(4-(imidazol-1-yl)phenyl)ethene (TIPE) as an electron-rich organic ligand with the π -conjugated tetraphenylethylene moiety and different silver salts were used to synthesize Ag-MOFs. A cubic Ag-MOF based on Ag-oxygen clusters, named as [Ag₈O₂(TIPE)₆](NO₃)₄ (**Ag-MOF1**), was obtained by using silver nitrate (AgNO₃). Meanwhile, silver trifluoromethanesulfonate (AgCF₃SO₃) and TIPE were utilized to synthesize an Ag-MOF, and [Ag(TIPE)_{0.5}CF₃SO₃] (**Ag-MOF2**) was obtained. The results show that **Ag-MOF2** has superior electrocatalytic performance for CO₂ reduction with high faradaic efficiency (FE) as well as high partial current density for CO compared with that of **Ag-MOF1**, implying that the MOF structure has great impact on electrocatalytic reduction of CO₂.

Experimental

Synthesis of [Ag₈O₂(TIPE)₆](NO₃)₄ (**Ag-MOF1**)

TIPE (0.05 mmol, 29.83 mg), 4,4'-oxybisbenzoic acid (H₂OBA) (0.1 mmol, 25.80 mg) and AgNO₃ (0.12 mmol, 20.40 mg) in a mixed solvent of 5 mL CH₃CN and 4 mL H₂O were added to a Teflon-lined stainless autoclave, which was heated at 160 °C for 56 h. The resulting mixture was cooled to ambient temperature and orange transparent cubic crystals were obtained in 35% yield based on TIPE. Anal. calcd for C₂₂₈H₁₆₈Ag₈N₅₂O₁₄: C, 57.98%; H, 3.59%; N, 15.42%. Found: C, 57.66%; H, 3.38%; N, 14.97%. IR (cm⁻¹, Fig. S1, ESI†): 3120 (m), 3043 (s), 1682 (s), 1602 (s), 1520 (w), 1491 (m), 1423 (s), 1355 (w), 1304 (m), 1254 (m).

Synthesis of [Ag(TIPE)_{0.5}CF₃SO₃] (**Ag-MOF2**)

TIPE (0.05 mmol, 29.83 mg) and AgCF₃SO₃ (0.12 mmol, 30.83 mg) in a mixed solvent of 8 mL CH₃CN and 4 mL H₂O were added to a Teflon-lined stainless autoclave, which was heated at 160 °C for 96 h. The resulting mixture was cooled to room temperature, and yellow transparent crystals were obtained in 81% yield based on TIPE. Anal. calcd for C₂₀H₁₄AgF₃N₄O₃S: C, 43.26%; H, 2.54%; N, 10.09%. Found: C, 42.97%; H, 2.32%; N, 9.76%. IR (cm⁻¹, Fig. S1, ESI†): 3118 (m), 1756 (s), 1602 (s), 1519 (w), 1420 (s), 1307 (s), 1263 (w), 1160 (m).

Electrochemical measurements and CO₂ reduction experiments

The catalyst (2 mg) was uniformly ground to a powder and dispersed into a mixed solution of 10 μ L of Nafion (5 wt%) and 190 μ L of isopropanol, then sonicated for 10 min to form a homogeneous ink. 200 μ L of the well-dispersed ink was loaded onto carbon paper (CP) with an area of 1 cm² and dried at 120 °C on a heating table. Electrochemical measurements were performed on a CHI 730E electrochemical workstation (Shanghai, Chenhua, China) using a three-channel flow cell comprising the Ag-MOF/CP as a working electrode, Pt as a

counter electrode and Ag/AgCl (saturated KCl electrolyte) as a reference electrode. For CO₂ reduction experiments, the cathode and anode chambers were separated by an anion exchange membrane (Fumasep, FAB-PK-130) while the electrolyte was 1 M KOH. The electrolyte in the cathode and anode was circulated by a peristaltic pump (Kamoer, F01A-STP) with a flow rate of 10 mL min⁻¹. High purity CO₂ (99.9995%) gas was continuously passed through the flow chamber with a flow rate of 20 mL min⁻¹ via a mass flow controller (Sevenstar, D07-7B). All potentials were measured *versus* an Ag/AgCl reference electrode (with saturated KCl) without *iR* compensation. The potentials were converted to the RHE scale using the following equation: $E(\text{versus RHE}) = E(\text{versus Ag/AgCl}) + 0.197 + 0.059 \times \text{pH}$. All experiments were carried out at room temperature.

Results and discussion

Crystal structures and characterization of Ag-MOFs

Ag-MOF1 was isolated by reaction of TIPE and AgNO₃ together with H₂OBA. It is noteworthy that no **Ag-MOF1** was obtained without addition of H₂OBA. This means that H₂OBA may play a role in the formation of **Ag-MOF1** although there is no H₂OBA in the formed **Ag-MOF1**. Single-crystal X-ray diffraction (SC-XRD) analysis revealed that **Ag-MOF1** belongs to cubic space group *P* $\bar{4}3n$ (Table 1). The asymmetric unit contains one twenty-fourth molecule of [Ag₈O₂(TIPE)₆](NO₃)₄ and there are Ag₄O clusters, in which each O²⁻ ion links four Ag(I) ions. Each Ag(I) is four-coordinated with distorted tetrahedral configuration and surrounded by one O²⁻ and three imidazole N-atoms from three different TIPE ligands (Fig. 1a). The Ag(1)–O(1) and Ag(1)–N(1) distances are of 2.5898(14) Å and 2.314(9) Å, respectively, and the corresponding angles around the Ag(I)

Table 1 Crystal data and structure refinements for **Ag-MOF1** and **Ag-MOF2**

Compound	Ag-MOF1	Ag-MOF2
CCDC	2311795	2311796
Empirical formula	C ₁₉ H ₁₄ Ag _{0.67} N _{4.33} O _{1.17}	C ₂₀ H ₁₄ AgF ₃ N ₄ O ₃ S
Formula weight	393.59	555.28
Crystal system	Cubic	Monoclinic
Space group	<i>P</i> $\bar{4}3n$	<i>C2/m</i>
Temperature/K	193	193
<i>a</i> /Å	17.2542(3)	13.9254(4)
<i>b</i> /Å	17.2542(3)	14.9602(5)
<i>c</i> /Å	17.2542(3)	11.7909(4)
β /°	90	119.6310(10)
Volume/Å ³	5136.7(3)	2135.13(12)
<i>Z</i>	12	4
<i>D_c</i> /g cm ⁻³	1.527	1.727
μ /mm ⁻¹	4.483	6.090
<i>F</i> (000)	2388	1104
Reflections collected	15 859	9034
Independent reflections	1885	2024
Goodness-of-fit	1.019	1.061
<i>R</i> ₁ ^a [<i>I</i> > 2 σ (<i>I</i>)]	0.0662	0.0567
<i>wR</i> ₂ ^b [<i>I</i> > 2 σ (<i>I</i>)]	0.1710	0.1616

^a $R_1 = \sum ||F_o| - |F_c|| / \sum |F_o|$. ^b $wR_2 = [\sum w(|F_o|^2 - |F_c|^2)^2 / \sum w(F_o)^2]^{1/2}$, where $w = 1/[\sigma^2(F_o^2) + (aP)^2 + bP]$. $P = (F_o^2 + 2F_c^2)/3$.

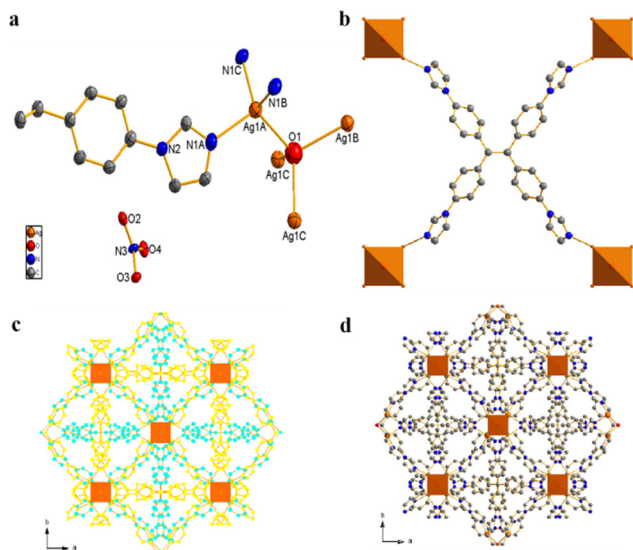


Fig. 1 (a) Coordination environment of Ag(I) in **Ag-MOF1** with the ellipsoids drawn at the 30% probability level. Hydrogen atoms are omitted for clarity. (b) Coordination environment of TIPE. (c) and (d) Interpenetrated 3D structures of **Ag-MOF1** along the *c*-axis. Free nitrate anions are omitted for clarity.

atom vary in the range of 106.8(2)–130.5(7)° (Table S1, ESI†), all of which coincide with those reported in the literature. Each TIPE ligand contains four imidazole N-atom donors and connects four Ag₄O clusters as a 4-connected node (Fig. 1b). Each Ag₄O cluster joins with 12 TIPE ligands, leading to 12-connected nodes. Thus, **Ag-MOF1** has a (4,12)-connected architecture. Moreover, owing to the action of the ligand and the bridge connection of metal ions, **Ag-MOF1** forms a two-fold interpenetrating three-dimensional (3D) framework (Fig. 1c and d). The void volume in **Ag-MOF1** is 208.5 Å³ calculated by PLATON, which is 4.1% of the unit cell volume (5136.7 Å³).

SC-XRD analysis shows that **Ag-MOF2** crystallizes in the monoclinic crystal system with *C2/m* space group (Table 1). The repeat unit of **Ag-MOF2** has a half molecule of [Ag(TIPE)_{0.5}CF₃SO₃]. Each Ag(I) is coordinated by two nitrogen atoms from two distinct TIPE ligands (Fig. 2a). Each TIPE links

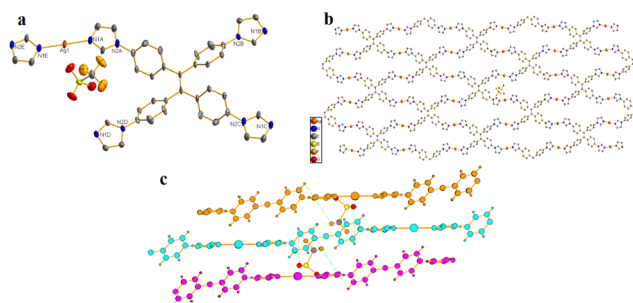


Fig. 2 (a) Coordination environment of Ag(I) in **Ag-MOF2** with the ellipsoids drawn at the 30% probability level. Hydrogen atoms are omitted for clarity. (b) 2D structure of **Ag-MOF2**. (c) 3D supramolecular structure of **Ag-MOF2** with hydrogen bonds indicated by dashed lines.

four Ag(I) atoms to form a two-dimensional (2D) layered structure of **Ag-MOF2** (Fig. 2b). The 2D layers are further connected by C–H⋯F and C–H⋯O hydrogen bonding interactions between TIPE and CF₃SO₃[−] to form a 3D supramolecular structure of **Ag-MOF2** (Fig. 2c). The results indicate that anions have a significant impact on the formation of Ag-MOFs.

Phase and morphology characterization of Ag-MOFs

The phase purity and chemical stability of Ag-MOFs were examined by powder X-ray diffraction (PXRD). As shown in Fig. S2 and S3, ESI†, PXRD patterns of the synthesized samples are in good agreement with the simulated ones, indicating that the synthesized bulky samples are consistent with the structures determined by SC-XRD. It is worth noting that the PXRD patterns of samples do not change significantly after immersion in 1 M KOH solution for 24 h, implying that the samples have high chemical stability in harsh alkaline environments. Fourier transform infrared (FT-IR) spectroscopic data show that the bands around 3000–3100 and 1400–1600 cm^{−1} correspond to the stretching vibrations of aromatic C–H and C=C bonds, respectively (Fig. S1, ESI†). The characteristic bands at 1254 and 1263 cm^{−1} are caused by the stretching vibration of the C–N bond. Compared with the TIPE ligand, the shifts of the band at 1254 cm^{−1} in **Ag-MOF1** and the one at 1263 cm^{−1} in **Ag-MOF2** caused by C–N bond vibration ensure the coordination between TIPE and Ag. The characteristic band at 1602 cm^{−1} is caused by the stretching vibration of the C=N bond.²⁵ In addition, the thermal stability of Ag-MOFs was estimated by thermogravimetric analysis (TGA). As shown in Fig. S4, ESI†, the stability of **Ag-MOF1** can be maintained up to 320 °C while **Ag-MOF2** can be stable up to 450 °C under an N₂ atmosphere.

Electrochemical CO₂RR performance

The CO₂RR behavior of the prepared samples was tested by using a standard three-electrode flow-cell system at room temperature in 1 M KOH. The experimental results presented in this work for all potential testing processes relative to the Ag/AgCl electrode are converted into reversible hydrogen electrode (RHE). As the voltage becomes more negative, the current gradually increases, which is mainly caused by two factors: one is the current generated by the hydrogen evolution reaction (HER), while the other is the current generated by electrocatalytic reduction of CO₂. In order to further test CO₂RR selectivity of the samples, we conducted FE testing. Gas chromatography analysis shows that CO and H₂ are the gas products, while no liquid products were detected in the ¹H NMR spectrum (Fig. S5, ESI†). From Fig. 3b, it can be seen that **Ag-MOF2** can reach the highest FE_{CO} of 92.21% at −0.98 V, and it is worth noting that the selectivity of CO for **Ag-MOF2** is over 80% within a wide potential range, indicating that the reduction effect of electrocatalytic CO₂ is superior to that of the HER. **Ag-MOF1** gives the maximum selectivity with 78.02% FE_{CO} at −1.08 V (Fig. 3a). In order to more clearly compare the selectivity of CO for Ag-MOFs, the FE_{CO} of Ag-MOFs under different potentials was displayed. As illustrated in Fig. 3c, **Ag-**

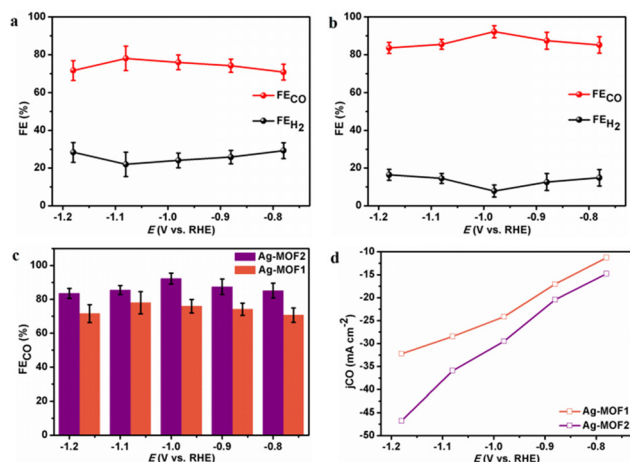


Fig. 3 (a) FEs of the HER and CO at different potentials for **Ag-MOF1**. (b) FEs of the HER and CO at different potentials for **Ag-MOF2**. (c) FEs of CO at different potentials for Ag-MOFs. (d) The partial current densities of CO for Ag-MOFs.

MOF2 achieves better selectivity for CO than **Ag-MOF1** when covering the tested potential range. The partial current density for the products was studied to further illustrate the CO₂RR performance of Ag-MOFs. Partial current density corresponding to CO (j_{CO}) for **Ag-MOF2** reaches 29.51 mA cm⁻² at -0.98 V (Fig. 3d). As exhibited in Fig. 3d, the absolute value of j_{CO} for **Ag-MOF2** is larger than that of **Ag-MOF1** at all the measured potentials. The results indicate that the structures of Ag-MOFs have great impact on their electrocatalytic properties for CO₂ reduction and that the 2D-layered structure of **Ag-MOF2** is more beneficial for the CO₂RR compared with the interpenetrated 3D framework of **Ag-MOF1**. Table S2, ESI† summarizes the performance comparison of the prepared Ag-MOFs with other catalysts used in the literature for CO₂ electroreduction to CO in terms of FE and current density. It can be seen that the FE_{CO} of Ag-MOFs is higher than that of catalysts such as [Al₂(OH)₂(Co(tcpp))], PCN-222-Fe and {Ag₄₉Mo₁₆}.^{26–28}

To uncover the origin of differences in the CO₂RR performance between **Ag-MOF1** and **Ag-MOF2**, CO₂ adsorption and further electrochemical measurements were conducted. The CO₂ adsorption isotherms reveal that **Ag-MOF2** has higher CO₂ adsorption capacity than **Ag-MOF1** (Fig. S6, ESI†). The electrochemical double-layer capacitance (C_{dl}) was determined by collecting cyclic voltammetry (CV) profiles in the non-faradaic region to investigate the electrochemical surface area (ECSA) of the catalysts. CV curves of each catalyst were recorded at different sweep speeds of 20, 40, 60, 80, 100 and 120 mV s⁻¹ in the non-pseudocapacitance region of -0.10–0 V vs. Hg/HgO (Fig. S7, ESI†). The current density difference, Δj , at a potential of -0.05 V vs. Hg/HgO was plotted with the corresponding sweep speed, and the k value is C_{dl} . The results show that C_{dl} increases in the order of **Ag-MOF1** < **Ag-MOF2** (Fig. 4a), which corresponds to the results of the electrochemical CO₂RR, indicating that **Ag-MOF2** with its large ECSA possesses more

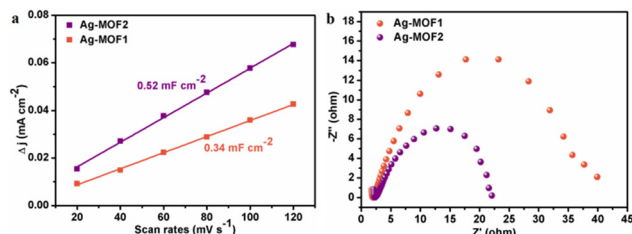


Fig. 4 (a) Electrochemical double-layer capacitance plots for Ag-MOFs. (b) Nyquist plots of Ag-MOFs.

exposed active sites, benefiting its electrochemical performance for the CO₂RR.²⁹ Electrochemical impedance spectroscopy (EIS) was used to estimate the rate of charge transfer and explore the kinetics of the CO₂ electroreduction reaction. The Nyquist plots show shapes of depressed semicircles corresponding to charge transfer reactance (Fig. 4b). The plot for **Ag-MOF2** exhibits a small curvature radius, proving that it has a fast charge transfer rate during the process of electrocatalysis. The low resistance of **Ag-MOF2** can speed up the transfer of electrons from the catalyst surface to the reaction intermediate, thus improving its catalytic activity and selectivity.³⁰

Evaluation of the electrochemical and structural stability of Ag-MOFs

The stability and tolerance of catalysts are important indicators that reflect their suitability for practical utilization. Therefore, we conducted current–time experimental tests on **Ag-MOF2** at a potential of -0.98 V vs. RHE. As shown in Fig. 5a, the current density of **Ag-MOF2** exhibits almost no change after running the electrocatalytic test for 6 h, indicating that **Ag-MOF2** has good electrochemical stability in 1 M KOH. We conducted PXRD tests on the catalyst after the electrocatalytic test, as shown in Fig. 5b and Fig. S8, ESI†. The PXRD patterns of Ag-MOFs after the CO₂RR test are basically consistent with the simulated ones, further proving that samples we prepared have electrochemical stability and tolerance, and can be used as stable and efficient CO₂ electroreduction catalysts. FT-IR spectra after the CO₂RR also support the conclusion that Ag-MOFs have good stability (Fig. S9 and S10, ESI†), although there are tiny Ag nanoclusters after electrolysis

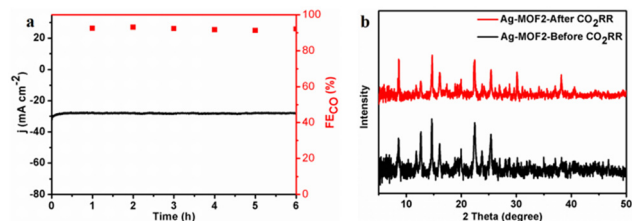


Fig. 5 (a) Total current density and FE of CO over 6 h of electrolysis at -0.98 V on the **Ag-MOF2** catalyst. (b) PXRD patterns of **Ag-MOF2** before and after the CO₂RR test.

reflected by transmission electron microscopy (TEM) measurements (Fig. S11, ESI†).

Conclusions

In summary, a stable Ag₄O cluster-based cubic **Ag-MOF1** and a 2D-layered **Ag-MOF2** have been synthesized and used for CO₂ electrocatalytic reduction. The selectivity to CO and H₂ of these Ag-MOFs is distinct. The results show that **Ag-MOF2** with high selectivity has a large electrochemically active surface area and fast electron transport rate, which may originate from its 2D-layered structure. In addition, the results of this work show that the N-enriched ligand with its π -conjugated system is unique due to its strong coordination ability with Ag(I) leading to Ag-MOFs with suitable stability for the CO₂RR, which is important for designing new Ag-MOFs for the CO₂RR.

Conflicts of interest

There are no conflicts to declare.

Acknowledgements

We gratefully acknowledge the National Natural Science Foundation of China (grant no. 22231006 and 22171131) for financial support of this work. This work was also supported by a Project Funded by the Priority Academic Program Development of Jiangsu Higher Education Institutions.

References

- 1 X. M. Lv, Z. Z. Liu, C. Yang, Y. L. Ji and G. F. Zheng, *Acc. Mater. Res.*, 2023, **4**, 264–274.
- 2 B. L. Yang, C. Shao, X. L. Hu, M. R. Ngata and M. D. Aminu, *Energy Fuels*, 2023, **37**, 1757–1776.
- 3 C. F. Xu, Y. L. Dong, H. P. Zhao and Y. Lei, *Adv. Funct. Mater.*, 2023, **33**, 2300926.
- 4 D. Sundar, C. H. Liu, S. Anandan and J. J. Wu, *Molecules*, 2023, **28**, 5383.
- 5 W. Y. Wang, K. Zhang, T. Xu and Y. G. Yao, *Dalton Trans.*, 2022, **51**, 17081–17088.
- 6 D. F. Wu, P. Z. Chen, D. M. Feng, J. J. Song and Y. Tong, *Dalton Trans.*, 2021, **50**, 14120–14124.
- 7 Y. Y. Guan, Y. Y. Liu, J. Yi and J. J. Zhang, *Dalton Trans.*, 2022, **51**, 7274–7283.
- 8 J. Y. Kim, Y. Kim, C. H. Ryu and H. S. Ahn, *Green Chem.*, 2023, **25**, 5290–5295.
- 9 Z. Y. Sun, T. Ma, H. C. Tao, Q. Fan and B. X. Han, *Chem*, 2017, **3**, 560–587.
- 10 Z. Xia, M. Freeman, D. X. Zhang, B. Yang, L. C. Lei, Z. J. Li and Y. Hou, *ChemElectroChem*, 2018, **5**, 215.
- 11 W. J. Zhang, Y. Hu, L. B. Ma, G. Y. Zhu, Y. R. Wang, X. L. Xue, R. P. Chen, S. Y. Yang and Z. Jin, *Adv. Sci.*, 2018, **5**, 1700275.
- 12 X. Q. Wang, Z. Chen, X. Y. Zhao, T. Yao, W. X. Chen, R. You, C. M. Zhao, G. Wu, J. Wang, W. X. Huang, J. L. Yang, X. Hong, S. Q. Wei, Y. E. Wu and Y. D. Li, *Angew. Chem., Int. Ed.*, 2018, **57**, 1944.
- 13 L. Z. Dong, Y. F. Lu, R. Wang, J. Zhou, Y. Zhang, L. Zhang, J. Liu, S. L. Li and Y. Q. Lan, *Nano Res.*, 2022, **15**, 10185–10193.
- 14 J. M. Lee, K. Otake and S. Kitagawa, *Coord. Chem. Rev.*, 2020, **421**, 213447.
- 15 R. B. Lin, S. C. Xiang, W. Zhou and B. L. Chen, *Chem*, 2020, **6**, 337–363.
- 16 X. Xiao, L. L. Zou, H. Pang and Q. Xu, *Chem. Soc. Rev.*, 2020, **49**, 301–331.
- 17 L. Feng, K. Y. Wang, G. S. Day, M. R. Ryder and H. C. Zhou, *Chem. Rev.*, 2020, **120**, 13087–13133.
- 18 Y. S. Wei, M. Zhang, R. Q. Zou and Q. Xu, *Chem. Rev.*, 2020, **120**, 12089–12174.
- 19 Y. Pan, R. Lin, Y. J. Chen, S. J. Liu, W. Zhu, X. Cao, W. X. Chen, K. L. Wu, W. C. Cheong, Y. Wang, L. R. Zheng, J. Luo, Y. Lin, Y. Q. Liu, C. G. Liu, J. Li, Q. Lu, X. Chen, D. S. Wang, Q. Peng, C. Chen and Y. D. Li, *J. Am. Chem. Soc.*, 2018, **140**, 4218–4221.
- 20 Y. Zhang, Q. Zhou, Z. F. Qiu, X. Y. Zhang, J. Q. Chen, Y. Zhao, F. Gong and W. Y. Sun, *Adv. Funct. Mater.*, 2022, **32**, 2203677.
- 21 U. Nwosu and S. Siahrostami, *Catal. Sci. Technol.*, 2023, **13**, 3740–3761.
- 22 C. B. Li, Y. A. Ji, Y. P. Wang, C. X. Liu, Z. Y. Chen, J. L. Tang, Y. W. Hong, X. Li, T. T. Zheng, Q. Jiang and C. Xia, *Nano-Micro Lett.*, 2023, **15**, 113.
- 23 Q. Lu, J. Rosen, Y. Zhou, G. S. Hutchings, Y. C. Kimmel, J. G. Chen and F. Jiao, *Nat. Commun.*, 2014, **5**, 3242.
- 24 D. H. Won, H. Shin, J. Koh, J. Chung, H. S. Lee, H. Kim and S. I. Woo, *Angew. Chem., Int. Ed.*, 2016, **55**, 9297.
- 25 K. I. Hadjiivanov, D. A. Panayotov, M. Y. Mihaylov, E. Z. Ivanova, K. K. Chakarova, S. M. Andonova and N. L. Drenchev, *Chem. Rev.*, 2021, **121**, 1286–1424.
- 26 N. Kornienko, Y. B. Zhao, C. S. Kiley, C. H. Zhu, D. Kim, S. Lin, C. J. Chang, O. M. Yaghi and P. D. Yang, *J. Am. Chem. Soc.*, 2015, **137**, 14129–14135.
- 27 B. X. Dong, S. L. Qian, F. Y. Bu, Y. C. Wu and Z. W. Li, *ACS Appl. Energy Mater.*, 2018, **1**, 4662–4669.
- 28 S. Q. Li, L. F. Dai, Y. Q. Tian, Y. X. Yi, J. Yan and C. Liu, *Chem. Commun.*, 2023, **59**, 575–578.
- 29 K. L. Yao, Y. J. Xia, J. Li, N. Wang, J. R. Han, C. C. Gao, M. Han, G. Q. Shen, Y. C. Liu, A. Seifitokaldani, X. H. Sun and H. Y. Liang, *J. Mater. Chem. A*, 2020, **8**, 11117–11123.
- 30 S. H. Chen, W. H. Li, W. J. Jiang, J. R. Yang, J. X. Zhu, L. Q. Wang, H. H. Ou, Z. C. Zhuang, M. Z. Chen, X. H. Sun, D. S. Wang and Y. D. Li, *Angew. Chem., Int. Ed.*, 2022, **61**, e202114450.